

# Enhancing Aluminium-Ion Battery Performance with Carbon Xerogel Cathodes

Paloma Almodóvar,<sup>[a]</sup> Natalia Rey-Raap,<sup>[b]</sup> Samanta L. Flores-López,<sup>[b]</sup> Belén Sotillo,<sup>[c]</sup> Lara Santos,<sup>[a]</sup> Miguel Tinoco,<sup>[d]</sup> Julio Ramírez-Castellanos,<sup>[d]</sup> Inmaculada Álvarez-Serrano,<sup>[d]</sup> María Luisa López,<sup>[d]</sup> Ignacio Cameán,<sup>[b]</sup> Ana Arenillas,<sup>[b]</sup> Joaquín Chacón,<sup>[a]</sup> and Ana B. García<sup>[b]</sup>

This study presents groundbreaking results in the field of rechargeable aluminium-ion batteries, achieving stable capacities exceeding  $300 \text{ mAh g}^{-1}$  for more than 300 cycles. The key to this achievement lies in the utilization of tailor-made carbon materials and a urea- $\text{AlCl}_3$ -based electrolyte. The article investigates the optimal physicochemical properties of the active material necessary for effective electrodes for these aluminium-ion batteries. This investigation employs a wide range of materials characterization techniques (XRD, SEM-EDX,  $\text{N}_2$  adsorption-desorption isotherms, Hg porosimetry, XPS, FTIR, Raman and TEM-EDX) and electrochemical performance analy-

ses to delve into the subject. These findings represent a significant improvement in the capacity of aluminium-ion batteries, bringing us closer to their implementation and commercialization. This achievement is attributed to the utilization of readily available, cost-effective, and non-corrosive materials. The ability to customize carbon xerogels and the use of the urea- $\text{AlCl}_3$  electrolyte offer promising avenues for the practical implementation of these advanced battery technologies, leading to further enhancements in their performance and widespread adoption in various applications.

## Introduction

Electrical energy storage devices have gained increasing attention due to the growing demand for mobility devices and renewable energy storage related applications. While lithium-ion batteries (LIBs) have served as the primary power source for portable electronics and electric vehicles, there is still substantial room for improvement in their performance and energy storage capabilities. This is where aluminium-ion batteries (AIBs) come into play, with the potential to revolutionize how we store and utilize energy.<sup>[1]</sup> AIBs are composed of a metallic aluminium anode, a carbonaceous material or a transition metal oxide cathode<sup>[2-4]</sup> and an electrolyte based on an ionic liquid capable of moving the redox active species ( $\text{AlCl}_4^-$  and  $\text{Al}_2\text{Cl}_7^-$ ). Among the various emerging energy storage system options, AIBs are positioned as a promising alternative to LIBs. Al anode presents a high theoretic gravimetric capacity ( $2980 \text{ Ah kg}^{-1}$ ),

low cost (Al bench market price is 2 USD/kg versus Li 300 USD/kg), great abundance (the most abundant metal in the earth's crust), and high safety.<sup>[5,6]</sup> However, for these batteries to become viable, three main identified problems need to be solved:

- (i) The limited specific cathode capacity. Currently, the best results obtained do not exceed  $200 \text{ mAh g}^{-1}$ .<sup>[3,7]</sup> This problem is related to the size and quantity of complex ions to be intercalated in the cathode.<sup>[8]</sup> To solve this drawback, it is necessary to search for new and more compatible cathode materials.
- (ii) The low cathode stability. Materials reported have, generally, low efficiency (~80%) and low capacity retention.<sup>[3,7]</sup>
- (iii) The corrosivity of chloroaluminate-based ionic liquids. Typically, varying mixtures of 1-ethyl-3-methylimidazolium chloride ([EMIm]) and  $\text{AlCl}_3$ , known as EMIC, are used. In fact, this corrosivity restricts the choice of materials for the separator (polyethylene), the binder (PVDF), the current collector (Al, stainless steel, Ni), and the cell casing. Thus, these electrolytes represent a significant increase in cell cost, not only due to the cost of the electrolyte itself but also to the cell adaptation required.<sup>[2,9,10]</sup> Therefore, a less corrosive electrolyte as well as more resistant materials (metal alloys, ceramics, polymers) must be developed and/or selected for these components.

In this work, an effective solution is proposed to produce an AIB with potential to become commercialized. This solution is based on the substitution of the EMIC by an electrolyte based on urea and  $\text{AlCl}_3$  and the use of carbon xerogels as cathode material. The potential use of this eutectic mixture as electrolyte in AIBs has been previously reported, since it has important

[a] P. Almodóvar, L. Santos, J. Chacón  
Zelestium Technologies, 42110, Soria, Spain  
E-mail: palmodov@ucm.es

[b] N. Rey-Raap, S. L. Flores-López, I. Cameán, A. Arenillas, A. B. García  
Instituto de Ciencia y Tecnología del Carbono, INCAR-CSIC, 33011, Oviedo, Spain

[c] B. Sotillo  
Departamento de Física de Materiales, Facultad de Física, Universidad Complutense de Madrid, 28040, Madrid, Spain

[d] M. Tinoco, J. Ramírez-Castellanos, I. Álvarez-Serrano, M. L. López  
Departamento de Química Inorgánica, Facultad de Química, Universidad Complutense de Madrid, 28040, Madrid, Spain

 Supporting information for this article is available on the WWW under <https://doi.org/10.1002/batt.202400114>

advantages over EMIC, i.e., ~50 times lower price, less corrosive and much more eco-friendly.<sup>[11,12]</sup> However, it has been observed that for the correct operation of this electrolyte it is necessary to look for cathode materials not only compatible with the redox species of chloroaluminates, but also with the subspecies of urea which are present in this electrolyte.<sup>[13–16]</sup>



Carbon materials, renowned for their low cost, wide availability, and diverse range of precursors, as well as their unique blend of electrical, mechanical, and physical properties, have found extensive application as electrode materials in metal-ion batteries,<sup>[17]</sup> including their utilization as cathodes in AIBs (Table S1). However, despite considerable efforts, the optimal properties required for carbon cathode materials in AIBs remain elusive. Furthermore, achieving reproducibility in carbon properties poses a significant challenge due to the inherent variability in precursor composition, typically sourced from biomass and/or fossil fuel waste. Hence, the strategic design and synthesis of synthetic carbons with high reproducibility and meticulously controlled properties emerge as the most viable approach. In this context, sol-gel technology enables the design of carbon materials with tailored properties,<sup>[18,19]</sup> allowing for control over porosity and chemical composition. Drawing on studies demonstrating the advantageous effects of nitrogen presence in cathode materials for AIBs,<sup>[20]</sup> and recognizing the significance of an appropriate pore size,<sup>[21]</sup> we have developed nitrogen-doped and undoped carbon xerogels to investigate their compatibility with the above mentioned electrolyte in order to develop a new optimized AIB. Additionally, it is crucial for the synthesis process to be both scalable and industrially applicable. Therefore, the primary objective of this study is to design and manufacture carbon xerogels through an optimized sol-gel process assisted by microwave heating, with improved electrochemical properties, including high capacity, high efficiency, and cycling stability for AIB cathodes.

This new aluminium-ion battery proposed not only exhibits high specific capacity values ( $>330 \text{ mAhg}^{-1}$ ), but also features high efficiency and capacity retention, low cost for all the materials used, and avoids system safety related issues.

## Experimental

### Synthesis of Carbon Xerogels

Two carbon xerogels with a pore size able to insert the redox active species (pore size  $>1000 \text{ nm} > \text{AlCl}_4^-$  ionic radius)<sup>[8,22]</sup> with different surface chemistry were designed by means of the polymerization of resorcinol (R, Indspec 99%) and formaldehyde (F, Merck 37% stabilized with 10 wt.% MeOH). The organic precursor was synthesized using the stoichiometric molar ratio (i.e., R/F = 0.5), a dilution ratio of 7.7 and a pH of the precursor mixture of 4.6. The precursor solution was placed in a microwave oven at 85 °C for 5 h, allowing

gelation, ageing and drying in the same device, according to a synthesis procedure previously optimized.<sup>[23]</sup> The resultant organic gel was carbonized in a tubular furnace at 1000 °C for 2 h under an inert atmosphere to obtain its carbon derivative CX.

A second nitrogen-doped carbon xerogel (CWN) was obtained. A portion of CX was powdered and subjected to an additional treatment in the presence of melamine at a weight ratio of CX: melamine of 60:40. The heat treatment was conducted at 700 °C for 2 hours under an inert atmosphere to introduce nitrogen surface functionalities on the carbon xerogel.

### Structural/Textural Characterization Techniques

CX and CWN materials were characterized by means of their porous properties and chemical composition. Prior to the characterization, both materials underwent vacuum outgassing overnight at 120 °C. The porous properties were determined using helium density (dHe, AccuPyc 1330), N<sub>2</sub> adsorption-desorption isotherms (Tristar II, Micromeritics), and Hg porosimetry (Autopore Micromeritics). The specific ( $S_{\text{BET}}$ ) and external ( $S_{\text{ext}}$ ) surface areas, as well as the micro-( $V_{\text{micro}}$ ) and mesopore ( $V_{\text{meso}}$ ) volumes were obtained from N<sub>2</sub> adsorption-desorption isotherms using the BET, t-plot, and Dubinin-Radushkevich equations. The macropore volume ( $V_{\text{macro}}$ ), pore size distribution, and mean pore size were determined from Hg porosimetry. Additionally, the morphology of the materials was characterized with a Quanta FEG 650 SEM working with an accelerating voltage of 20 kV. Furthermore, chemical and structural characterizations were performed by energy-dispersive X-ray spectroscopy (EDX) coupled to SEM; elemental analysis; X-ray photoelectron spectroscopy (XPS); X-ray powder diffraction (XRD); Micro-Raman; and infrared spectroscopy (FTIR). Scanning electron microscopy (SEM) images were obtained in a FEI Inspect-S SEM instrument. Energy dispersive X-ray microanalysis (EDX) elemental mappings were acquired with a QUANTAX 70 detector (Bruker, Berlin, Germany) attached to a Hitachi TM3000 SEM microscope working at 15 kV. XPS analysis was performed in a SPECS PHOIBOS 100 using a monochromate Al source. XRD patterns were measured at room temperature with a PANalytical X'PERT POWDER diffractometer using Cu K $\alpha$  radiation ( $\lambda = 1.5418 \text{ \AA}$ ). Micro-Raman measurements were carried out at room temperature in a Horiba Jobin-Yvon LabRAM HR800 on an Olympus BX 41 confocal microscope system with a 633 nm He-Ne laser. The FTIR spectra were collected in ATR using a ThermoNicolet-6700 FT-IR spectrometer equipped with a MCTA detector.

The electrical conductivity of the carbon xerogels was determined using disk-shaped electrodes. For the preparation of these electrodes, a powdered sample of the xerogels is mixed with 10 wt.% of polytetrafluoroethylene (PTFE) as the binder to obtain a homogeneous mixture. The mixture is worked to obtain a film that is cut and pressed uniaxially into circular electrodes of 1 cm diameter. The four-point probe procedure (FPP, model SR-4-6L, Ever-being) is performed by applying a constant current (model 6220 DC current source, Keithley) while the four in-line points and the surface of the disk-shaped electrodes are in contact. The voltage drop is measured using a digital voltmeter (model 2182 A, Keithley) thus quantifying the electrical resistance of the material. Finally, from the electrical resistance, the conductivity is calculated using Van der Pauw's equation.

### Cell Preparation and Electrochemical Techniques

The electrochemical tests were performed at room temperature in 13 mm diameter Swagelok-type cells (PTFE cell body and Mo plungers) assembled in an Ar-filled dry box, using graphite paper

(Carbon-Foil, Goodfellow) with the same diameter as current collector (for both negative and positive electrodes). An Al metal foil (99.99%, Nature Alu) of 13 mm diameter was employed as the negative electrode, while a Whatman GF/D borosilicate glass fiber sheet, saturated with a mixture of urea (crystalline urea, Fertiberia) and  $\text{AlCl}_3$  (99%, Sigma Aldrich) 1:1.5 by mol, was used as electrolyte. The volume of electrolyte corresponds to one-fourth of the deposited cathode material, measured in mL (i.e.,  $\sim 0.25 \text{ mL}/\text{mg}$ ). For the cathode, the carbon xerogel (CX or CXN) was mixed in a battery slurry mixer at a rotation speed of 300 rpm for 1 h with carbon SP (Carbon black, Imerys) and sodium alginate (Sigma Aldrich) as conductive additive and binder, respectively, in deionised water. The obtained slurry was uniformly applied onto graphite paper using an automated Battery Electrode Film Coating Machine at a fixed height of 100  $\mu\text{m}$ . Subsequently, the coated electrodes were dried overnight at 40  $^{\circ}\text{C}$ . Cathodes with a diameter of 13 mm and a targeted material loading of approximately 5 mg ( $\sim 4 \text{ mg cm}^{-2}$ ) were prepared. Electrodes with various weight ratios of active material and binder, with and without carbon black, were prepared and labelled based on the type of carbon xerogel (CX or CXN), the weight percentages of binder ( $x_B$ ) and carbon black ( $y_{CB}$ ). Thus, electrodes without carbon black would be denoted as CXxB or CXNxN, while CXxByCB or CXNxByCB would represent electrodes containing both binder and carbon black. For better comparison of the results and a more realistic estimation from an application perspective, all per-gram values correspond to the total weight of material deposited on the current collector, i.e., active carbon material + conductive additive + binder. It is important to underscore that the graphite paper used as current collector does not actively partake in the electrochemical processes observed in the cathode, as substantiated by prior investigations.<sup>[4]</sup>

Charge-discharge cycling, and cyclic voltammetry experiments were performed using an Arbin BT-2143 Battery Tester potentiostat. The measurements were conducted in a voltage range between 0.4 V and 2.4 V to assess the electrochemical performance of the system (voltage limits in which the response of the Urea- $\text{AlCl}_3$  electrolyte has been proven to be stable).<sup>[14]</sup> During charge-discharge experiments, the cells were subjected to a constant current, including 100, 200, 500, and 1000  $\text{mA g}^{-1}$ , to evaluate their energy storage capabilities. Cyclic voltammograms (CVs) were obtained by sweeping the voltage at different scan rates (1, 2, 5, 10, and 20  $\text{mV s}^{-1}$ ) within the specified voltage range, after completing five charge/discharge cycles to ensure the stabilization of the electrochemical system and obtain better-defined profiles.

Electrochemical Impedance Spectroscopy (EIS) data were acquired using a Biologic BCS-810 battery tester by applying an AC voltage of 5 mV over a frequency range of 0.01 to 100 kHz. The acquired data were subsequently analysed using the BTS-Lab software. The EIS measurements were conducted under two conditions: open-circuit voltage (OCV) and charged (2.4 V) after five charge-discharge cycles.

### Ex-Situ Electrode Characterization

For the ex-situ characterization of the electrodes, the cells were disassembled in an Ar-filled dry box, and the electrodes were cleaned with n-butanol. The ex-situ measurements were always performed after completing different charge/discharge protocols, with the number of cycles varying depending on the specific study.

Ex-situ Transmission electron microscopy (TEM) coupled with EDX was performed in a JEOL JEM 2100 located at the facilities of the ICTS-Centro Nacional de Microscopía Electrónica, operating at an acceleration voltage of 200 kV. The samples were prepared by crushing the electrode powder under n-butanol and dispersing it

over copper grids covered with a holey carbon film. The *ex-situ* FTIR measurements were performed using a Perkin Elmer Spectrum Two instrument equipped with an attenuated total reflectance (ATR) accessory with a diamond window and a LiTaO<sub>3</sub> detector, in the wavenumber range of 350 to 4000  $\text{cm}^{-1}$ . The electrodes were placed directly onto the window, and pressure was applied using the arm of the instrument to ensure good contact between the electrode sample and the ATR window.

## Results and Discussion

### Textural and Chemical Properties of Carbon Xerogels

The textural properties of CX and CXN carbons are summarized in Table 1. Both materials have a similar helium density ( $\rho_{\text{He}}$ ) around  $2 \text{ g cm}^{-3}$ , which is a very common value for carbon xerogels treated under similar thermal conditions. Moreover, as can be appreciated in Figure 1a, both samples show a characteristic adsorption-desorption isotherm of micro-macroporous materials (i.e., type II).<sup>[24]</sup> However, differences in the profiles were observed among them. CX presents a higher  $N_2$  adsorbed volume at low relative pressure than CXN, which is attributed to its higher surface area and microporosity (i.e. defect in the structure). As reflected in Table 1,  $V_{\text{micro}}$  and  $S_{\text{BET}}$  decrease from 0.24 to  $0.09 \text{ cm}^3 \text{g}^{-1}$  and 632 to  $221 \text{ m}^2 \text{g}^{-1}$ , respectively, by effect of the treatment with melamine applied. Moreover, at higher relative pressure, CXN shows an H4 hysteresis loop, which indicates a slight increase in the mesoporosity of this material. Such differences are in good agreement with previous reports on the variation of textural properties in carbon materials doped with melamine.<sup>[25]</sup> These reports have shown that using temperatures below 750  $^{\circ}\text{C}$  for grafting nitrogen on the surface of carbon materials, results in blocking microporosity of the carbon support and the formation of mesopores due to the presence of subproducts from the decomposition and further recombination of melamine.

On the other hand, CX carbon was confirmed to have a macroporous nature through Hg porosimetry. This material exhibited a  $V_{\text{macro}}$  of  $2.71 \text{ cm}^3 \text{g}^{-1}$  (Table 1) and a main pore size centred at 1142 nm (Figure 1b). The Hg intrusion method is unable to determine the main macropore size in powdered samples, such as CXN. However, based on the comparable values of the specific external surface area ( $S_{\text{ext}}$ ) of the materials

Table 1. Textural properties of CX and CXN carbon xerogels.

	CX	CXN
$\rho_{\text{He}} (\text{g cm}^{-3})$	2.08	2.04
$S_{\text{BET}} (\text{m}^2 \text{g}^{-1})$	632	221
$S_{\text{ext}} (\text{m}^2 \text{g}^{-1})$	11	16
$V_{\text{micro}}^{[a]} (\text{cm}^3 \text{g}^{-1})$	0.24	0.09
$V_{\text{meso}}^{[a]} (\text{cm}^3 \text{g}^{-1})$	0.03	0.04
$V_{\text{macro}}^{[b]} (\text{cm}^3 \text{g}^{-1})$	2.71	N.D. <sup>[c]</sup>

[a] From  $N_2$  adsorption-desorption isotherm. [b] From Hg porosimetry. [c] N.D. non-determined.

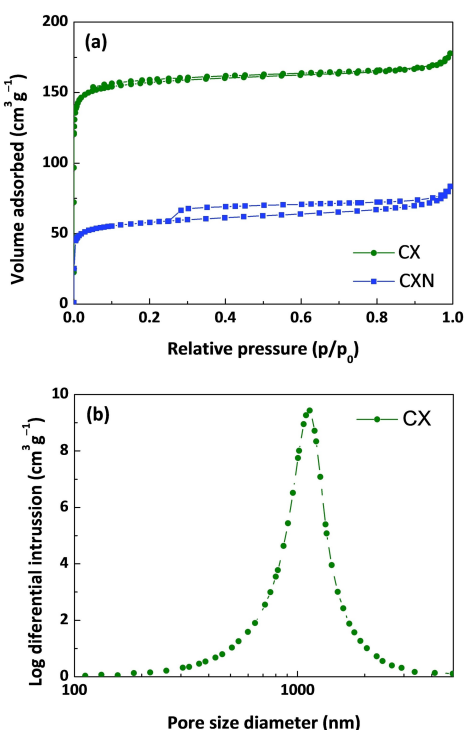


**Figure 1.** (a)  $\text{N}_2$  adsorption-desorption isotherms at  $-196^\circ\text{C}$  of CX and CXN and (b) Pore size distribution of CX.

(Table 1) and the shape of the isotherms near the saturation point (i.e.,  $p/p^0=1$ , Figure 1a), it can be inferred that the treatment applied for the introduction of nitrogenated species did not alter the macropore structure in the CXN material.

Furthermore, to corroborate this fact, SEM characterization (Figures 2a–b) reveals that CX and CXN materials have a

comparable nodular morphology, with polymer clusters of similar size, that would give rise to an analogous macroporosity in both samples.

In summary, the carbon xerogels CX and CXN exhibit a macropore size of approximately  $1\text{ }\mu\text{m}$ , promoting favourable electrolyte diffusion, along with similar external surface area (indicating similar most accessible surface) but different degrees of microporosity (i.e. structural defects) that has been identified as a factor influencing on carbon materials electrochemical response because of its interaction with the active redox species.<sup>[18,26]</sup> It is imperative to strike a balance, as the pore size must be sufficiently large to enable the insertion and extraction of active species, yet excessively large sizes may be counter-productive, leading to the accumulation of  $\text{AlCl}_4^-$  and subsequent undesired reactions among them.<sup>[21]</sup>

In good agreement with the bulk elemental analysis (Table S2), the semi-quantitative results from EDX analysis (Figures 2c–d) show that CX primarily consists of carbon (C) with a composition of approximately 94.3 wt.% / 95.7 at.%, along with a small signal indicating the presence of oxygen (5.7 wt.% / 4.3 at.%) (Figure 2c). On the other hand, in CXN, the oxygen content decreases (3.6 wt.% / 2.7 at.%), while the dominant signal is still carbon (90.9 wt.% / 92.5 at.%). Additionally, a new signal for nitrogen is observed (5.5 wt.% / 4.8 at.%) in CXN, indicating its presence in the doped carbon xerogel (Figure 2d). The EDX mapping further confirms the homogeneous distribution of nitrogen within CXN (inset Figure 2d). Importantly, no signals of other elements were found in any of the materials, demonstrating the absence of impurities in their composition.

XPS results present the same trend in the material's composition. CX only contains 93 at. % C and 7 at. % O. Whilst in the case of CXN, the composition comprises a similar content for C (92.5 at.%), lower oxygen content (4.1 at.%), and 3.4 at. % of nitrogen. It is noteworthy that the oxygen content reported by XPS is higher than in the EDX and bulk elemental analysis, which suggest that oxygen concentrates on the surface. This observation is crucial for understanding any surface interactions. Table S3 and Figure 3 present the deconvolution results of the detected elements (i.e., C, O, and N) in the carbon xerogels. The deconvolution of the N1s band indicates that nitrogen was introduced in CXN as different functional groups: pyridinic (398.6 eV), pyrrolic (400.2 eV), graphitic (401.0 eV), and oxidized species (403 eV).<sup>[24,26,27]</sup> Among them, pyridinic nitrogen was detected in much higher proportion (Table S3), which is consistent with previous reports on carbon materials doped with nitrogen compounds.<sup>[25,27,28]</sup> The analysis of the O1s band reveals a significant decrease in oxygen content in CXN, suggesting that nitrogen was primarily introduced through interaction with oxygenated groups on the surface of CX. However, both carbon xerogels exhibit a similar distribution of oxygen in  $\text{O}=\text{C}$  (~25.5%, 531.5 eV),  $\text{O}-\text{C}$  (~43%, 532.3 eV) and  $\text{OC}=\text{O}$  (~30%, 534 eV) species. Additionally, the deconvolution of the C1s band for both materials shows a very similar profile, as the signals of the oxygen and nitrogen bonds coincide at the same binding energy. These signals include  $\text{C}-\text{O}/\text{C}-\text{N}$  eV,  $\text{C}=\text{O}/\text{C}=\text{N}$  and  $\text{COO}/\text{N}-\text{C}(\text{N})-\text{N}$  at 286–286.7, 286.7–287.5 and 288.5–

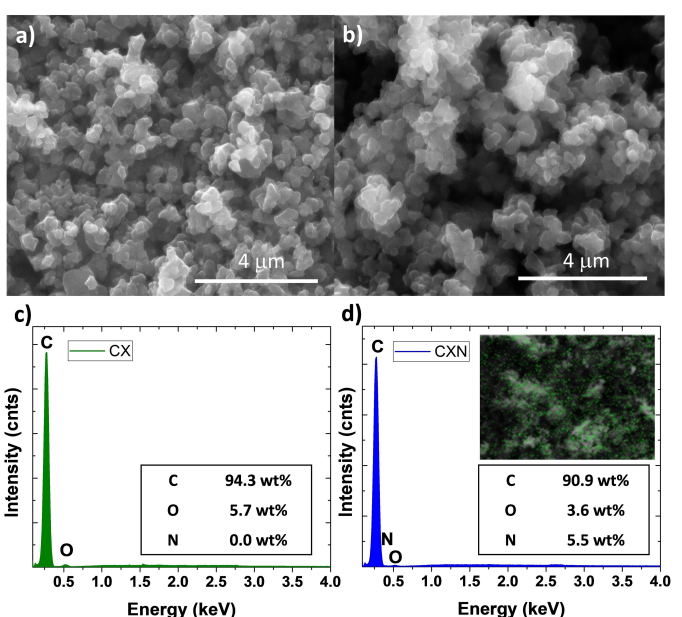


**Figure 2.** SEM images and EDX chemical composition of (a,c) CX and (b,d) CXN carbon xerogels. Mapping inset in d) corresponds to N distribution in CXN.

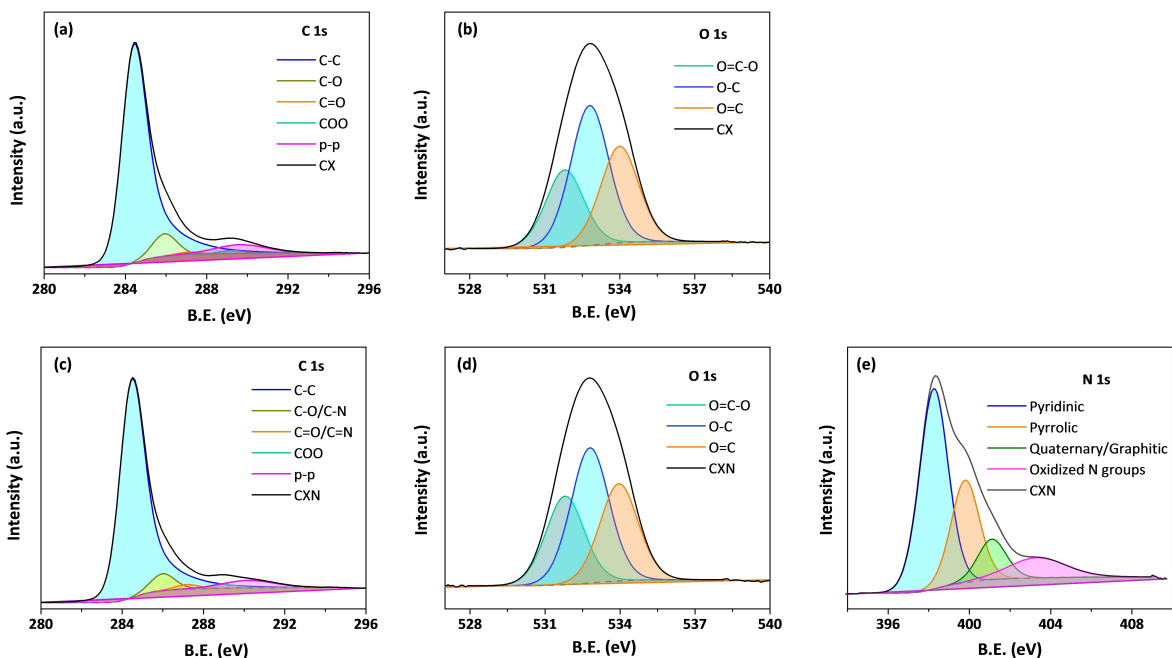


Figure 3. XPS profiles and deconvolution of C1s, O1s, and N1s bands obtained from XPS analysis of CX (a, b) and CXN (c, d, e) carbon xerogels.

289 eV, respectively.<sup>[27,29,30]</sup> However, the higher signals at around 287 and 289 eV, show the introduction of C=N and N–C(N)–N functionalities.

The structural characterization of the carbon xerogels, CX and CXN, was completed using XRD, FTIR, and Raman measurements (Figure S1). The XRD patterns exhibited broad peaks at around 20 of  $\sim 26^\circ$  and  $\sim 44^\circ$ , corresponding to (002) and (100) reflections (PDF 00-001-0646), respectively, indicating their carbon amorphous nature (Figure S1a).<sup>[31]</sup> This amorphous nature is further supported by Raman measurements (Figure S1c), in which the carbon characteristic D and G bands (located at  $\sim 1320$  and  $\sim 1600\text{ cm}^{-1}$ , respectively) show pronounced broadening. It is noteworthy that the nitrogen-doped sample has a more disordered and defective character, thus featuring a broad band centred at  $\sim 2700\text{ cm}^{-1}$ .<sup>[32]</sup> This band aligns with the presence of the nitrogen groups detected through XPS, known to induce defects in carbon structures upon doping.<sup>[20]</sup> Furthermore, the FTIR spectra (Figure S1b) confirmed the presence of nitrogen species on the surface of CXN, with additional peaks corresponding to triazine species (at  $804\text{ cm}^{-1}$ ),<sup>[22]</sup> CN stretching vibrations (at 1010, 1210 and  $1396\text{ cm}^{-1}$ ),<sup>[20]</sup> and C=N bonds (at ca.  $1500\text{ cm}^{-1}$ ). The high-temperature carbonization process resulted in fewer functional groups on the surface of CX. Only C–O stretching vibrations around  $1000\text{ cm}^{-1}$  and C=O stretching vibration from carboxylic acids at  $1500\text{ cm}^{-1}$  are detected. This observation agrees with the less disordered structure observed in Raman analysis.

### Electrochemical Performance of Carbon Xerogels as Cathodes

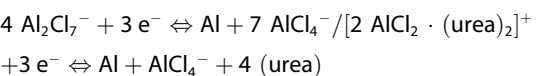
Initially, the electrodes were prepared without carbon black conductive additive, with a weight ratio of active material:

binder (sodium alginate) of 90:10. It is worth mentioning that sodium alginate was selected as the binder due to its ability to enhance the intercalation of  $\text{AlCl}_4^-$  ions in carbonaceous cathode materials, leading to increased specific capacities.<sup>[33]</sup> Additionally, the use of this binder also promotes a safer and more environmentally friendly battery manufacturing process by eliminating the need for toxic solvents like NMP.

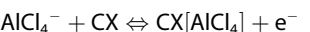
These electrodes were labelled as CX10B and CXN10B, respectively. Figure 4a shows the CVs of the batteries, at a scan rate of  $1\text{ mVs}^{-1}$ , using CX10B and CXN10B as cathodes. As seen, both electrodes present similar redox peaks at 2.1 V, 1.7 V and 1.2 V, which have been previously ascribed to intercalation, the first one, and deintercalation, the other two, of the active chloroaluminates species in graphitic-based cathodes of Al-ion batteries with urea-based electrolytes.<sup>[14,34]</sup> However, compared to these cathodes, the redox peaks in CX10B and CXN10B appear less defined.

Therefore, it can be assumed that the electrochemical reactions accepted for graphitic materials also occur in both carbon xerogel-based cells:

#### Negative electrode reaction



#### Positive electrode reaction



Among the two xerogels-based cathodes, it can be noticed that CXN10B shows larger area enclosed in its CV. This result starts to highlight the better electrochemical performance of the nitrogen-doped xerogel as cathode material for AIBs when

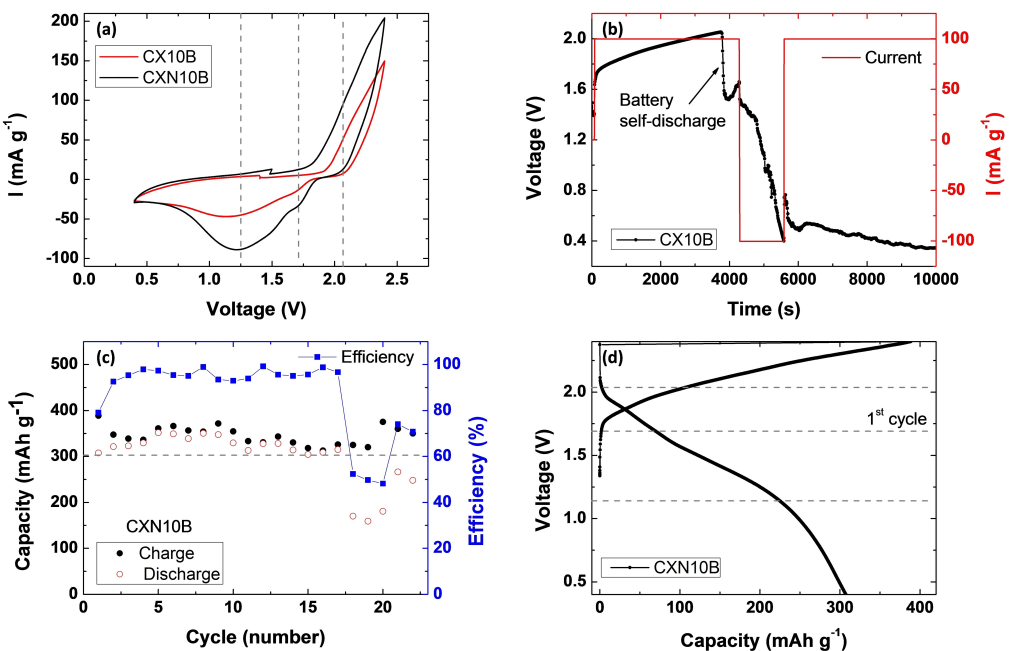


**Figure 4.** (a) CVs at  $1 \text{ mVs}^{-1}$  for CX10B and CXN10B, (b) Voltage and current vs. time plots for CX10B charging/discharging protocol, (c) Specific capacity and coulombic efficiency vs. cycle number, at  $100 \text{ mA g}^{-1}$ , for CXN10B in the  $0.4\text{--}2.4 \text{ V}$  voltage range and (d) First cycle charge-discharge voltage curves vs. specific capacity for CXN10B, at  $100 \text{ mA g}^{-1}$ .

the urea-based electrolyte is used. This observation aligns with recently conducted density functional theory (DFT) calculations, revealing that even a low presence of nitrogen groups enhances the binding energy between the cathode active material and  $\text{AlCl}_4^-$  redox active species. The stronger this binding, the more facile it becomes for  $\text{AlCl}_4^-$  to overcome van der Waals forces and intercalate into the active material.<sup>[20]</sup>

Figure 4b shows the charge and discharge curves of CX10B cathode at a current density of  $100 \text{ mA g}^{-1}$ . It can be observed that CX material is not able to complete even one entire charge since it starts to self-discharge when it reaches  $\sim 2.1 \text{ V}$ , even by applying current. Although CX material has a considerable number of defects (i.e., microporosity, see Table 1) for the interaction with  $\text{AlCl}_4^-$  active species, the stability of the electrode is far from satisfactory (Figure 4b). After the first complete discharge, this electrode appears to be totally damaged, not even being able to recover its open-circuit voltage. These results suggest an interaction CX-electrode/electrolyte not favourable. It is noteworthy that this evaluation was repeated multiple times, without observing any significant improvement in the results.

In Figure 4c, the specific capacity and efficiency versus cycle number plots are presented for the electrochemical system using CXN10B as cathode, with cycling conducted for 25 cycles at a current density of  $100 \text{ mA g}^{-1}$ . In contrast to CX, CXN exhibits remarkable stability, maintaining a capacity of over  $300 \text{ mA h g}^{-1}$  throughout the cycling process with a coulombic efficiency exceeding 95%. Figure 4d shows the voltage versus specific capacity profile for the initial charge-discharge cycle, revealing poorly defined plateaus consistent with earlier observations in the CVs.

These results clearly demonstrate the determinant role of the nitrogen functionalities present in CXN. However, there is limited research on whether different nitrogen functionalities in carbon materials have an equal impact on the interaction with  $\text{AlCl}_4^-$ . According to a recent theoretical study,<sup>[20]</sup> pyridinic and graphitic nitrogen produce a strength interaction with  $\text{AlCl}_4^-$ , thereby reducing the formation of  $\text{Al}_2\text{Cl}_7^-$  and  $\text{Cl}$  or  $\text{Cl}_2$ . This leads to increased storage capacity and reduced emission of chlorine, which may produce a further degradation of the electrode. Based on these studies, the significant pyridinic and graphitic nitrogen portions (more than 60% of the total nitrogen content, Table S3) present in CXN are likely responsible for its excellent electrochemical performance as compared to that of nitrogen-free CX counterpart.

Moreover, this excellent performance surpasses that of any previously reported cathode material with the same electrolyte (Table S1), highlighting the good behaviour and great potential of CXN to be considered an effective material in aluminium-ion batteries. However, as the cycling progresses, a decline in efficiency and a degradation are observed at around cycle 18 (Figure 4c). This may be attributed to the inherent low electrical conductivity of the CXN material (Table S4) or the poor CXN10B electrode mechanical stability (the continuous anion storage can gradually deteriorate the electrode, leading to a loss of contact between particles).<sup>[28,31,35]</sup>

Considering the results obtained without an electric conductive additive, new cathodes based on CXN were prepared incorporating different carbon black (CB) contents to enhance the electrochemical stability and enable them to withstand a higher number of cycles. It has to be taken into accounts that CB is not only a conductive additive but also contributes to the

adhesion of the particles in the electrode, improving its consistency and durability. The best proportion of CB was found to be 25 wt %. Moreover, the quantities of CXN active material and binder (sodium alginate) were varied. Cathodes with weight percentages of 45% CXN, 30% binder, and 25% carbon black (denoted as CXN30B25CB) and 55% CXN, 20% binder, and 25% carbon black (denoted as CXN20B25CB) were found to exhibit the best electrochemical performance as regards capacity and cycling efficiency (Figure 5).

It is important to note that carbon black was also subjected to electrochemical characterization in the same conditions, using an electrode composed of carbon black and sodium alginate in a 90:10 weight ratio (Figure S2), to evaluate its individual contribution. As depicted in Figure S2, this additive shows a maximum capacity of  $28 \text{ mAh g}^{-1}$  in the first cycle, followed by a continuous capacity decrease and complete degradation after a few cycles. These results dismiss a significant involvement of carbon black in the storage processes of the redox active species, confirming its main role as a conductive material, in addition to its contribution to the conformation of the electrode.

Comparing the CVs of the new CXN30B25CB and CXN20B25CB electrodes (containing the active material CXN, binder and CB) in Figure 5a with that of CXN10B electrode (without CB), it can be inferred that the electrochemical mechanism does not change, i.e., the redox peaks are practically in the same positions (no significant changes of more than 0.1 V are detected in any peak). This observation is corroborated by the similarity of the voltage profiles of the three electrodes (Figure 5b).

Figures 5c–d present the capacity and coulombic efficiency profiles as a function of the number of cycles for the CXN-based

cathodes containing carbon black. Comparing these results with those in Figure 4c, it is evident that the addition of carbon black to the cathode, along with an increase in the binder proportion, significantly enhances its electrochemical stability, consistently delivering capacity values of  $\geq 200 \text{ mAh g}^{-1}$  throughout the cycling process. Notably, CXN20B25CB (Figure 5d) stands out, providing capacity values exceeding  $300 \text{ mAh g}^{-1}$  with efficiencies  $> 95\%$  for almost all of the cycling period (300 cycles). Approximately between cycles 50 and 75, a gradual small decrease in capacity is observed for this electrode. However, it underwent a rapid recovery of its initial capacity and subsequently stabilized again, highlighting the CXN material's remarkable ability to readjust its structure and maintain excellent electrochemical stability within this system. The only difference between CXN20B25CB and CXN30B25CB electrodes is the binder content and therefore the percentage of active material in the electrode. Indeed, increasing the content of the active material in the electrode would result in a higher capacity for the overall system (Figure 5c–d).

From these results, it is evident that the addition of conductive carbon black is necessary to enhance, among others, the electrical conductivity of the electrode. Additionally, the binder plays a crucial role in providing consistency and durability to the electrode structure. Optimizing the proportions of the different cathode components by finding the right balance between active material, conductive additive, and binder is essential for the good operation of the ALBs. This optimization process aims to achieve a composition that combines high capacity and cycling stability, good conductivity, and mechanical stability, ultimately leading to improved ALB performance.

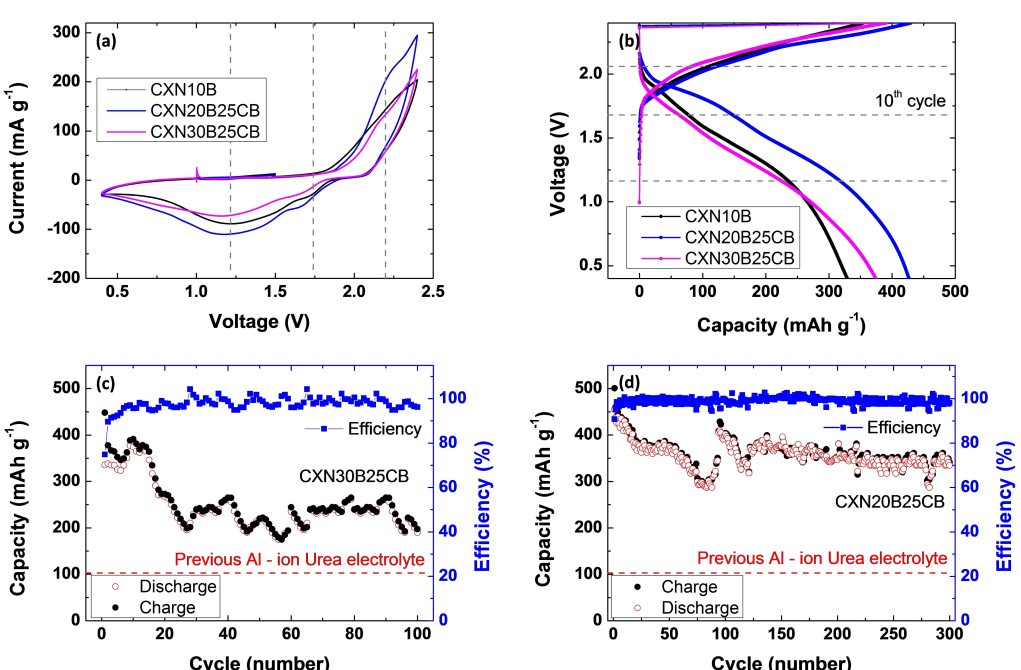


**Figure 5.** (a) CVs at  $1 \text{ mVs}^{-1}$  and (b) charge-discharge voltage curves vs. capacity of cycle #10 at  $100 \text{ mA g}^{-1}$  for CXN10B, CXN20B25CB and CXN30B25CB cathodes, and (c), (d) specific capacity and coulombic efficiency vs. cycle number at  $100 \text{ mA g}^{-1}$  for CXN30B25CB and CXN20B25CB cathodes, respectively.

As mentioned above, the capacity values determined for CXN-based cathodes surpass those previously reported for AlBs using carbon materials cathodes in urea-based electrolytes, which typically do not exceed  $100 \text{ mAh g}^{-1}$  with lower efficiency values (Table S1). Moreover, in the case of CXN20B25CB cathode, the capacity increase is over three times higher. This significant improvement emphasizes the potential of developing high-capacity batteries using cost-effective materials, without the need to rely on lithium-ion batteries. To gain further insights into the excellent electrochemical performance of the CXN-based electrode (Figure 5d), the cell was opened, and the cathode was subjected to TEM-EDX analysis (Figure S3) following the charge/discharge cycling. After more than 300 cycles, both the morphology and crystal structure of the CXN material remain intact, further substantiating its high electrochemical stability in urea based AlBs. The only notable difference observed was the detection of Al and Cl through EDX analysis after cycling, which is likely attributed to the presence of chloroaluminates species.

CXN20B25CB cathode (Figure 5d) was further subjected to cycling at different current densities to assess its rate capability. Figure 6a illustrates the variation of specific capacity and

efficiency versus cycle number, with an increasing current density and returning to the initial value of  $100 \text{ mA g}^{-1}$ . As expected, an increase in current density from 100 to  $1000 \text{ mA g}^{-1}$  results in a gradual decrease in the cathode capacity. However, even at  $200 \text{ mA g}^{-1}$ , a capacity of  $\sim 200 \text{ mAh g}^{-1}$  with an efficiency above 95% was achieved. Once again, these capacity values surpass those previously reported for any material in this type of battery when cycling at current densities higher than  $100 \text{ mA g}^{-1}$ .<sup>[12,14,34]</sup> Furthermore, it is worth noting that this electrode exhibits excellent recovery properties upon returning to  $100 \text{ mA g}^{-1}$  (Figure 6), providing discharge capacity values of  $355 \text{ mAh g}^{-1}$  with an efficiency close to 100%, indicating that no cathode degradation occurred.

Furthermore, CV tests were conducted at different scan rates on the CXN20B25CB electrode (Figure S4a) to explore the insertion mechanisms in the main redox peaks. With increasing scan rates, the redox peaks located at  $\sim 2.1 \text{ V}$  (intercalation) and  $\sim 1.2 \text{ V}$  (deintercalation) showed an increase and shifted to higher/lower voltages, respectively. These observations align with the relationship described by the equation  $i = av^b$ , where  $i$  represents the measured current,  $v$  is the scan rate, and  $a$  and  $b$  are adjustable parameters. The  $b$  parameter reflects the slope of the linear line obtained by plotting  $\log i$  versus  $\log v$ , with values typically ranging from 0.5 to 1.0. A  $b$  value close to 0.5 indicates diffusion-controlled intercalation, while a value close to 1.0 suggests predominantly (pseudo)capacitive processes.<sup>[36]</sup> Regression analysis (Figure S4b) revealed values of  $0.5 < b < 0.6$  in both cases, indicating mechanisms primarily governed by diffusion-controlled processes, with some contribution from pseudocapacitive behaviour. This is consistent with the previously observed mechanisms of intercalation/deintercalation of  $\text{AlCl}_4^-$  ions into/from the carbon xerogels.<sup>[26]</sup>

For comparison, the electrochemical performance of CX material (without nitrogen) was also investigated using the same optimal electrode formulation, denoted as CX20B25CB. The specific capacity and efficiency versus cycle numbers can be found in Figure S5. It was observed that the addition of carbon black and an increase in the binder content allowed for the completion of several cycles with high efficiency ( $> 95\%$ ), which was not achieved previously (as seen in Figure 4b). However, unlike CXN20B25CB, the capacity values provided by the CX-based cathode did not exceed  $40 \text{ mAh g}^{-1}$ . These values are similar to those previously reported for other carbon-based cathodes in AlBs.<sup>[12,14,34]</sup> Therefore, while the addition of carbon black and binder clearly improved the electrochemical performance of the carbon xerogels materials studied, they alone do not explain the exceptional results achieved by using CXN material as the cathode. Nor does the greater microporosity (i.e., defects content) present in CX material, which could have somehow interacted with the  $\text{AlCl}_4^-$  species, seem decisive. In summary, the presence of nitrogen functionalities appears to be the key for the optimization of cathodes performance in AlBs.

To investigate the electrochemical processes occurring in the different electrodes, electrochemical impedance spectroscopy (EIS) measurements were conducted on the CX10B,

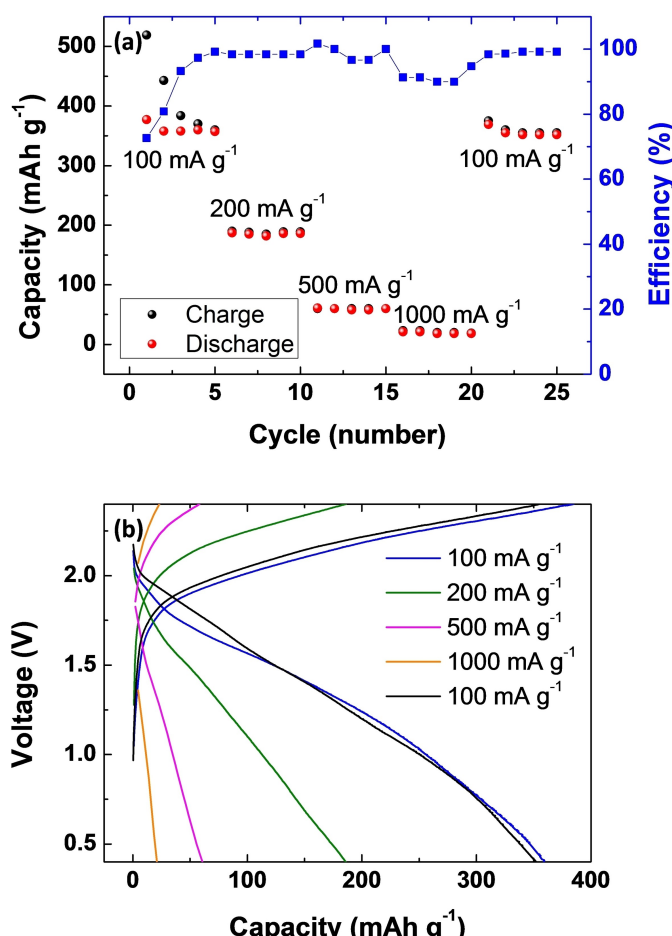


**Figure 6.** (a) Specific capacity and efficiency versus cycle number at increasing current density (from  $100$  to  $1000 \text{ mA g}^{-1}$ , and back to  $100 \text{ mA g}^{-1}$ ) and (b) representative voltage profiles for each applied current density, for CXN20B25CB cathode.

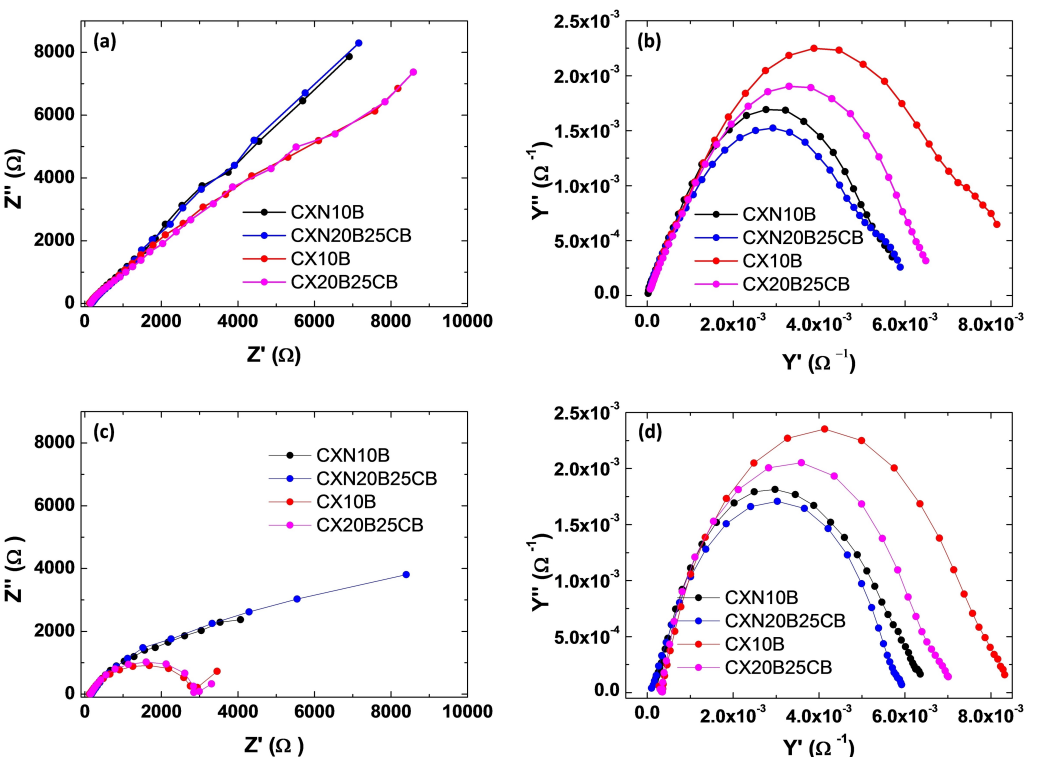


**Figure 7.** Nyquist impedance and admittance of the electrodes under the following conditions: open-circuit voltage (OCV) (a–b) and charged after 5 charge-discharge cycles (c–d).

CXN10B, CX20B25CB, and CXN20B25CB cathodes. The Nyquist impedance and admittance for all of them were analysed during both Open Circuit Voltage (OCV) and once the electrode was charged after completing five charge-discharge cycles. Interestingly, they exhibited similar behaviour in the initial OCV state (Figure 7a–b). The corresponding impedance plots showed a nearly linear trend with minimal initial semicircles. This characteristic indicates a reduced resistance at the electrode-electrolyte interface and efficient charge transfer kinetics.

However, the CXN-containing electrodes stood out with a steeper slope in this linear region, suggesting an even lower resistance at the interface. This observation was corroborated when analysing the admittance curves, which exhibited smaller semicircles for these CXN-containing electrodes. The presence of smaller semicircles suggests improved charge transfer processes, highlighting enhanced accessibility of reactants to the active sites on the electrode surface.<sup>[37,38]</sup> After 5 cycles, the EIS analysis revealed distinct behaviour among the electrodes (Figures 7c–d). The CX-based exhibited well-defined semicircles in their impedance plots, indicating a certain level of resistance at the electrode-electrolyte interface. In contrast, the CXN-cathodes showed a more linear nature in their impedance plots, accompanied by smaller semicircles in the admittance curves.<sup>[37,38]</sup>

Moreover, these findings strongly support that the presence of nitrogen in the electrode active material proved to be instrumental in enhancing charge transfer kinetics and reducing resistance at the electrode-electrolyte interface. Consequently,

it leads to higher battery capacity and significantly enhanced the overall battery performance.

To gain further insight into the differences between CX- and CXN-based cathodes performance, CX20B25CB and CXN20B25CB were analysed by FTIR after completing 5 full charge-discharge cycles and the obtained spectra are given in Figure 8. By comparing the spectra of the cycled cathodes with those of the original CX and CXN materials (Figure S1), it becomes evident that, in addition to the characteristic peaks previously observed in these samples within the range of 550 to 1550 cm<sup>-1</sup> (shown within the grey dashed box), new peaks associated with both urea and the active redox species emerge. Mainly at 3400–3500 cm<sup>-1</sup> and 1560 cm<sup>-1</sup>, the bands corresponding to urea from the electrolyte are clearly bigger for

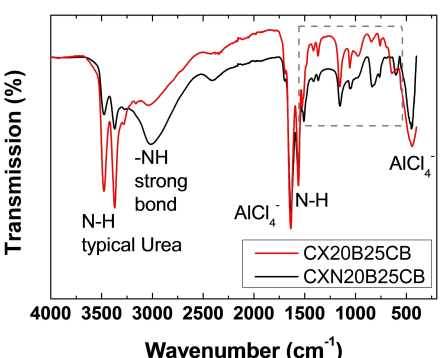


**Figure 8.** FTIR spectra of CX20B25CB and CXN20B25CB discharged electrodes after 5 full charge/discharge cycles.

CX20B25CB electrode. Similarly, the bands at  $1700\text{ cm}^{-1}$  and  $500\text{ cm}^{-1}$ , corresponding to the  $\text{AlCl}_4^-$  seems to be also bigger in the case of CX20B25CB. These facts can only be justified by a higher retention of these electrolyte species by the CX material, probably because it exhibits higher microporosity than CXN (see Table 1).<sup>[39–44]</sup> This microporous structure in combination with the low binding strength of carbon with  $\text{AlCl}_4^-$ , may allow the reaction of electrolyte species minimizing the storage capacity of the material.<sup>[19]</sup> Furthermore, these findings are corroborated by EDX spectra of these electrodes (Figure S6). It is evident that CX20B25CB exhibits a significantly higher aluminium and chlorine concentration compared to the CXN20B25CB. This discrepancy indicates the pronounced retention of redox-active species, leading to their interaction and the generation of  $\text{Cl}_2$ . This phenomenon aligns with previous postulations derived DFT analyses: Nitrogen doping increases the binding energies without creating any significant energy barrier for  $\text{AlCl}_4^-$  mobility, reducing the formation of  $\text{Al}_2\text{Cl}_7^-$  and  $\text{Cl}^-$ .<sup>[20]</sup>

Besides, for CXN20B25CB, an additional band appears at  $3030\text{ cm}^{-1}$  which is associated with  $-\text{NH}$  bonds, indicating a CXN/electrolyte interaction that is not present in CX20B25CB (Fig. 8). These findings lend support to the hypothesis that nitrogen in cathode materials improves the electrochemical performance among active materials in AIBs utilizing urea-based electrolytes, as previously suggested in other studies.<sup>[11,12,19]</sup>

## Conclusions

In this work, the electrochemical performance of a rechargeable aluminium-ion battery (AIB) has been optimized based on carbon xerogels as active material for the cathode. These carbon materials are cost-effective and easy to produce with tailored properties able to fit any specific requirements. The AIB presented here uses a non-corrosive urea-based electrolyte, which, in combination with a nitrogen-doped carbon xerogel, results in high specific capacities and efficiencies. Results proved that the presence of nitrogen in the xerogel significantly enhances the battery performance (up to one order of magnitude higher).

Furthermore, the optimal operation of these batteries has been observed under low current densities, where the intercalation and deintercalation processes are totally effective. This leads to a stable capacity of  $335\text{ mAhg}^{-1}$  over 300 cycles, with an efficiency exceeding 95% at a current density of  $100\text{ mA g}^{-1}$ . These results surpass the limitations of low capacities previously obtained in these kinds of batteries.

Overall, this work demonstrates the great potential of carbon xerogels doped with nitrogen together with a urea-based electrolyte to achieve remarkable performance improvements in aluminium-ion batteries, positioning them as a strong candidate in the energy storage market.

## Acknowledgements

The authors would like to thank Imerys Graphite & Carbon and Fertiberia who kindly provided us with the carbon black and the urea used in this work. The authors are also indebted to UCM XRD CAI centre and to the ICTS-CNME facilities. This research was funded by the Ministerio de Ciencia e Innovación de España, the European Union Next Generation EU/PRTR and Science, Technology and Innovation Plan2018–2022 of the Principado de Asturias with the projects PCI2020-112039 MCIN/AEI-10.13039/501100011033, PID2020-113001RB-I00 MCIN/AEI-10.13039/501100011033 and IDI/2021/50921. N. R.-R. is grateful to the Horizon-MSCA-2021-PF-01-01 call for financial support through the Metgel project 101059852. S. L. F.-L. thanks their PhD grant from “Severo Ochoa” Program of the Principado de Asturias.

## Conflict of Interests

The authors declare no conflict of interest.

## Data Availability Statement

The data that support the findings of this study are available from the corresponding author upon reasonable request.

**Keywords:** Al-ion battery • rechargeable • cathode • carbon xerogel • nitrogen

- [1] M. R. Chakraborty, S. Dawn, P. K. Saha, J. B. Basu, T. S. Ustun, *Batteries* **2022**, *8* (9), 124, <https://doi.org/10.3390/batteries8090124>.
- [2] Y. Liu, Q. Sun, W. Li, K. R. Adair, J. Li, X. Sun, *Green Energy & Environ.* **2017**, *2*, 246–277, <https://doi.org/10.1016/j.gee.2017.06.006>.
- [3] G. A. Elia, K. V. Kravchyk, M. V. Kovalenko, J. Chacón, A. Holland, R. G. A. Wills, *J. Power Sources* **2021**, *481*, 228870, <https://doi.org/10.1016/j.jpowsour.2020.228870>.
- [4] P. Almodóvar, D. A. Giraldo, J. Chacón, I. Álvarez-Serrano, M. L. López, *ChemElectroChem.* **2020**, *7*, 2102–2106, <https://doi.org/10.1002/celc.202000425>.
- [5] Q. Li, N. J. Bjerrum, *J. Power Sources* **2002**, *110* (1), 1–10, [https://doi.org/10.1016/S0378-7753\(01\)01014-X](https://doi.org/10.1016/S0378-7753(01)01014-X).
- [6] T. Leisegang, F. Meutzner, M. Zschornak, W. Münchgesang, R. Schmid, T. Nestler, R. A. Eremin, A. A. Kabanov, V. A. Blatov, D. C. Meyer, *Front. Chem.* **2019**, *7*, 1–21, <https://doi.org/10.3389/fchem.2019.00268>.
- [7] Z. Yang, F. Wang, P. Meng, J. Luo, C. Fu, *Energy Storage Mater.* **2022**, *51*, 63–79, <https://doi.org/10.1016/j.ensm.2022.06.018>.
- [8] D. Y. Wang, C. Y. Wei, M. C. Lin, C. J. Pan, H. L. Chou, H. A. Chen, M. Gong, Y. Wu, C. Yuan, M. Angell, Y. J. Hsieh, Y. H. Chen, C. Y. Wen, C. W. Chen, B. J. Hwang, C. C. Chen, H. Dai, *Nat. Commun.* **2017**, *8*, 14283, <https://doi.org/10.1038/ncomms14283>.
- [9] Z. Yu, S. Jiao, S. Li, X. Chen, W. L. Song, T. Teng, J. Tu, H. Sen Chen, G. Zhang, D. N. Fang, *Adv. Funct. Mater.* **2019**, *29*, 1–9, <https://doi.org/10.1002/adfm.201806799>.
- [10] Y. Song, S. Jiao, J. Tu, J. Wang, Y. Liu, H. Jiao, X. Mao, Z. Guo, D. J. Fray, *J. Mater. Chem. A* **2017**, *5*, 1282–1291, <https://doi.org/10.1039/C6TA09829K>.
- [11] P. Almodóvar, D. Giraldo, C. Díaz-Guerra, J. Ramírez-Castellanos, J. M. González Calbet, J. Chacón, M. L. López, *J. Power Sources* **2021**, *516*, 230656, <https://doi.org/https://doi.org/10.1016/j.jpowsour.2021.230656>.
- [12] M. Angell, C. J. Pan, Y. Rong, C. Yuan, M. C. Lin, B. J. Hwang, H. Dai, *Proc. Natl. Acad. Sci. USA* **2017**, *114*, 834–839, <https://doi.org/10.1073/pnas.1619795114>.

- [13] M. Angell, G. Zhu, M. C. Lin, Y. Rong, H. Dai, *Adv. Funct. Mater.* **2020**, *30*, 1–11, <https://doi.org/10.1002/adfm.201901928>.
- [14] M. Malik, K. L. Ng, G. Azimi, *Electrochim. Acta* **2020**, *354*, 136708, <https://doi.org/10.1016/j.electacta.2020.136708>.
- [15] G. Zhu, M. Angell, C. J. Pan, M. C. Lin, H. Chen, C. J. Huang, J. Lin, A. J. Achazi, P. Kaghazchi, B. J. Hwang, H. Dai, *RSC Adv.* **2019**, *9*, 11322–11330, <https://doi.org/10.1039/C9RA00765B>.
- [16] F. Jach, M. Wassner, M. Bamberg, E. Brendler, G. Frisch, *ChemElectroChem* **2021**, *8*, 1988–1992, <https://doi.org/10.1002/celec.202100183>.
- [17] Y. Yang, J. Zhou, A. M. Rao, B. Lu, *Nanoscale* **2024**, *16*, 5893–5902, <https://doi.org/10.1039/D4NR00226A>.
- [18] N. Cuesta, I. Cameán, A. Arenillas, A. B. García, *Microporous Mesoporous Mater.* **2020**, *308*, 110542. <https://doi.org/10.1016/j.micromeso.2020.110542>.
- [19] L. dos Santos-Gómez, N. Cuesta, I. Cameán, S. García-Granda, A. B. García, A. Arenillas, *Electrochim. Acta* **2022**, *426*, 140790, <https://doi.org/10.1016/j.electacta.2022.140790>.
- [20] S. Debnath, M. Horschek-diaz, D. J. Searles, M. Hankel, *Carbon* **2021**, *183*, 546–559, <https://doi.org/10.1016/j.carbon.2021.07.041>.
- [21] S. Debnath, C. Phan, D. J. Searles, M. Hankel, *CS Appl. Energy Mater.* **2020**, *3* (8), 7404–7415, <https://doi.org/10.1021/acsaeem.0c00805>.
- [22] D. Lee, G. Lee, Y. Tak, *Nanotechnology* **2018**, *29*, 1–9, <https://doi.org/10.1088/1361-6528/aacd7f>.
- [23] N. Rey-Raab, J. A. Menéndez, A. Arenillas, *Carbon* **2014**, *78*, 490–499, <https://doi.org/10.1016/j.carbon.2014.07.030>.
- [24] M. Thommes, K. Kaneko, A. Neimark, J. Olivier, F. Rodriguez-Reinoso, J. Rouquerol, K. Sing, *Pure Appl. Chem.* **2015**, *87*, 1052–1069, <https://doi.org/10.1515/pac-2014-1117>.
- [25] A. Öztürk, A. Bayrakçeken Yurtcan, *J. Solid State Chem.* **2021**, *296*, 121972. <https://doi.org/https://doi.org/10.1016/j.jssc.2021.121972>.
- [26] M. Eckert, H. Suthar, J. Drillet, *Materials* **2022**, *15* (7), 2597, <https://doi.org/10.3390/ma15072597>.
- [27] M. Ayiania, M. Smith, A. J. R. Hensley, L. Scudiero, J.-S. McEwen, M. García-Perez, *Carbon* **2020**, *162*, 528–544, <https://doi.org/https://doi.org/10.1016/j.carbon.2020.02.065>.
- [28] L. Ouyang, J. Xiao, H. Jiang, S. Yuan, *Molecules* **2021**, *26* (17), 5293. <https://doi.org/10.3390/molecules26175293>.
- [29] M. Inagaki, M. Toyoda, Y. Soneda, T. Morishita, *Carbon* **2018**, *132*, 104–140, <https://doi.org/https://doi.org/10.1016/j.carbon.2018.02.024>.
- [30] F. A. Permatasari, H. Fukazawa, T. Ogi, F. Iskandar, K. Okuyama, *ACS Appl. Nano Mater.* **2018**, *1*, 2368–2375, <https://doi.org/10.1021/acsanm.8b00497>.
- [31] M. Canal-Rodríguez, A. Arenillas, S. F. Villanueva, M. A. Montes-Morán, J. A. Menéndez, *Materials* **2020**, *13* (1), 119, <https://doi.org/10.3390/ma13010119>.
- [32] S. Kundu, I. H. Chowdhury, M. K. Naskar, *ACS Omega* **2018**, *3*, 9888–9898, <https://doi.org/10.1021/acsomega.8b01252>.
- [33] Z. Yang, M. Guo, P. Meng, M. Jiang, X. Qiu, J. Zhang, C. Fu, *Chem. A Eur. J.* **2023**, *29*, e202203546. <https://doi.org/https://doi.org/10.1002/chem.202203546>.
- [34] H. Jiao, C. Wang, J. Tu, D. Tian, S. Jiao, *Chem. Commun.* **2017**, *53*, 2331–2334, <https://doi.org/10.1039/c6cc09825h>.
- [35] M. Canal-Rodríguez, A. Arenillas, N. Rey-Raab, G. Ramos-Fernández, I. Martín-Gullón, J. A. Menéndez, *Carbon* **2017**, *118*, 291–298, <https://doi.org/https://doi.org/10.1016/j.carbon.2017.03.059>.
- [36] J. H. Xu, T. Schoetz, J. R. Mcmanus, V. R. Subramanian, W. Fields, R. J. Messinger, *J. Electrochem. Soc.* **2021**, *168*, 60514, <https://doi.org/10.1149/1945-7111/ac0648>.
- [37] B. Silwana, C. der Horst, E. Iwooha, V. Somerset, *Thin Solid Films* **2015**, *592*, 124–134, <https://doi.org/10.1016/j.tsf.2015.09.010>.
- [38] Z. Lukács, T. Kristóf, *Electrochim. Acta* **2020**, *363*, 137199, <https://doi.org/https://doi.org/10.1016/j.electacta.2020.137199>.
- [39] M. Manivannan, S. Rajendran, A. A. Nagar, *Int. J. Eng. Sci. Technol.* **2011**, *3* (11), 8048–8060.
- [40] X.-G. Sun, Y. Fang, X. Jiang, K. Yoshii, T. Tsuda, *Chem. Commun.* **2015**, *52*, 292–295, <https://doi.org/10.1039/C5CC06643C>.
- [41] Y. P. Patil, R. Kore, S. P. Kelley, R. D. Rogers, *Chem. Commun.* **2017**, *53*, 5449–54522, <https://doi.org/10.1039/C7CC01754E>.
- [42] K. Minsik, S. Hwang, J. Yu, *J. Mater. Chem.* **2007**, *17*, 1656–1659, <https://doi.org/10.1039/b702213a>.
- [43] R. Kore, S. P. Kelley, P. Aduri, R. D. Rogers, *Dalton Trans.* **2018**, *47*, 7795–7803, <https://doi.org/10.1039/C8DT00976G>.
- [44] N. R. Smyrl, G. Mamantov, L. E. Mccurry, *J. Inorg. Nucl. Chem.* **1978**, *40* (8), 1489–1492, [https://doi.org/10.1016/0022-1902\(78\)80456-4](https://doi.org/10.1016/0022-1902(78)80456-4).

Manuscript received: February 21, 2024

Revised manuscript received: May 6, 2024

Accepted manuscript online: May 7, 2024

Version of record online: June 27, 2024